



# Effect of Particle Mass Fraction on the Multiscale Dynamic Failure Behavior of Particulate Polymer Composites

S. Ravindran<sup>1</sup> · V. Gupta<sup>1</sup> · A. Tessema<sup>1</sup> · A. Kidane<sup>1</sup>

Received: 16 November 2018 / Accepted: 26 February 2019 / Published online: 28 March 2019  
© Society for Experimental Mechanics 2019

## Abstract

In this study, the effect of particle mass fraction on the dynamic multiscale behavior of particulate polymer composite is investigated. High spatiotemporal resolution digital image correlation-based experiments are conducted to understand the local deformation and the failure mechanisms. The deformation fields at different length scales are compared to each other to understand the link between macroscale and mesoscale behavior. All the experiments are carried out on polymer bonded sugar, a well-known mechanical simulant of polymer bonded explosives, with varying particle mass fraction. The transition of the soft binder dominated stress-strain behavior to a quasi-brittle type behavior was observed as the particle mass fraction is increased. The mesoscale experiments show that in samples with lower mass fraction, the deformation is mainly controlled by the binder. Whereas, at a higher mass fraction, the crystals are engaged in the load transferring process through the formation of force chain in the material. The formation of the force chain causes stress concentration followed by a brittle failure mode.

**Keywords** Energetic material · Particulate composite · Dynamic experiments · Mesoscale · PBX · PBS

## Introduction

The primary objective of this study is to understand the effect of mass fraction of crystals on the multiscale deformation and failure behavior of particulate polymer composites. Multiscale experiments are performed with the help of Hopkinson bar, ultra high-speed and high-magnification imaging and digital image correlation (DIC) technique on polymer bonded sugar (PBS) specimens. PBS is a popular simulant for polymer bonded explosives (PBXs), a class of particulate polymer composites widely used in solid propellants, explosive charges, civil applications, etc. PBXs typically consist of a high-mass fraction of explosive crystals (75–96%) and a small volume fraction of soft binder [1, 2]. The binder holds the particles together and at the same time reduces the sensitivity to dynamic loads.

The mechanical behavior of PBX is very complex due to several heterogeneities such as high volume fraction of the crystal compared to the matrix, microscale voids and cracks, significant mismatch in the properties of their constituents,

etc. [3–10]. Such materials can undergo loading conditions of varying timescales during transport, machining, storage, etc. Their sensitivity to dynamic loading is directly related to the local deformation and damage evolution that occurs at the corresponding loading conditions [3, 11–13]. In some cases, it was observed that, even at low impact velocity insults, localized high-temperature regions called hotspots are formed which causes an explosion at a pressure below the threshold shock [14, 15]. This poses a significant safety hazard during handling and transportation of polymer bonded energetic materials. Therefore, the understanding of multiscale material behavior under dynamic loading is critical in predicting the behavior and reliability of the material.

A great deal of numerical and experimental investigation has been done in the past in order to understand and predict the behavior of PBXs under different loading conditions [5, 16–22]. However, the needed multiscale experiments are scarce due to difficulty in characterizing the material at high magnification and faster time scales [21]. Recently, in-situ dynamic mesoscale experiments, based on DIC, have been successfully implemented to measure local deformation in heterogeneous materials at the order of 10  $\mu\text{m}/\text{pixel}$  and up to 5 million frames/s [23–26]. These studies revealed that the primary failure mechanisms under intermediate strain rate (150/s) loading conditions are de-bonding of the polymer binder and crystal fracture [23–26]. The observed local crystal

✉ A. Kidane  
kidanea@cec.sc.edu

<sup>1</sup> Department of Mechanical Engineering (Room A132), University of South Carolina, 300 Main Street, Columbia, SC 29208, USA

fracture in the PBX [23] was supported by the synchrotron X-ray studies on a model material with a few high melting explosive (HMX) crystals embedded in hydroxyl-terminated polybutadiene (HTPB) binder [27]. The research suggests that the observed crystal failure in the sample is mainly due to the tensile stress resulted from the force transfer between the crystals through crystal-to-crystal contacts [27]. It is clear that the contact between crystals highly depends on the mass fraction of the crystals in the composite system. In this work, the effect of crystal's mass fraction on the failure behavior of polymer composite is investigated by varying the mass fraction of crystals.

## Materials and Methods

### Material Preparation

Cold pressed PBS, a mechanical surrogate of PBX was used in this study. The simulant contains sugar crystals in place of explosive crystals in the material. This material has been extensively used to understand the deformation and failure behavior of PBXs [23, 24, 28]. The main reason for the selection of sugar as the surrogate is that its monoclinic crystal structure is the same as that of HMX. In this study, sugar crystals of size varying from 200 to 600  $\mu\text{m}$  were used to prepare the sample. Plasticized hydroxyl-terminated polybutadiene (HTPB), a well-known soft binder was used as a matrix in the explosive formulation. The binder was prepared by mixing HTPB, dioctyl sebacate (DOS) and toluene diisocyanate (TDI) in the mass proportion shown in Table 1. Three set of PBS samples were prepared by varying the mass fraction of the particles constituent (filler) in the material. These specific mass fractions are chosen in this study to cover the range of mass fraction in real explosives composition in which the explosive solid mass fraction varies between 75 and 96% [1, 2]. Specimens are named as PBS-80, PBS-87, and PBS-95 depending on the particle mass fraction used in the material. The detailed steps for sample preparation are described in [23]. By measuring the density, it was found that the porosity in the samples range between 8.5–10%.

**Table 1** Material constituents and compositions of the polymer bonded sugar

Sample	Sugar (%)	HTPB (%)	DOS (%)	TDI (%)
PBS-80	80.00	14.4	3.80	1.80
PBS-87	87.50	9.00	2.41	1.09
PBS-95	95.00	3.60	0.96	0.45

### Experimental Setup, Specimen Geometry, and Data Analysis

The dynamic compression experiments were performed in a split Hopkinson pressure bar (SHPB) setup at room temperature. A complete schematic diagram and the photograph of the experimental setup is shown in Fig. 1(a). The low impedance specimens in this study necessitate the use of a low impedance polycarbonate bar to obtain measurable transmitted signal during loading. Therefore, the incident, transmitter and striker bars used in this study are made of impact resistant polycarbonate material. Both incident and transmitter bars are 1830 mm long and 25.4 mm in diameter.

The duration and amplitude of the incident pulse were controlled by the length of the striker bar and the striker bar velocity respectively. Strain gauges were mounted in the middle of the incident and transmitter bar. They were connected to an oscilloscope (Tektronix DPO3034) through a signal conditioning amplifier (Vishay 2310). The strain gages, with resistance of 350  $\Omega$  and gage factor of 2.13, were purchased from OMEGA®. Wave dispersion and attenuation effects can be significant in non-metallic bars. Polycarbonate bars are viscoelastic in nature, and the wave attenuates and disperses as it propagates along the bar. Hence, the loading wave on the specimen may not be the same as that of the measured signal at some distance away from the specimen. The dispersion and attenuation of the loading wave are dependent on its frequency content. Thus, the signal can be corrected easily in the frequency domain using fast Fourier transform and then converted back to time domain for further analysis. The propagation coefficient for the polycarbonate bar was calculated using the strain data from a separate experiment conducted without the specimen. Then the propagation coefficient was used for correcting the incident, transmitted and reflected signals based on the procedure outlined in [29]. The average strain rate, strain, and stress in the specimen were calculated from the corrected signal using the following well-known equations,

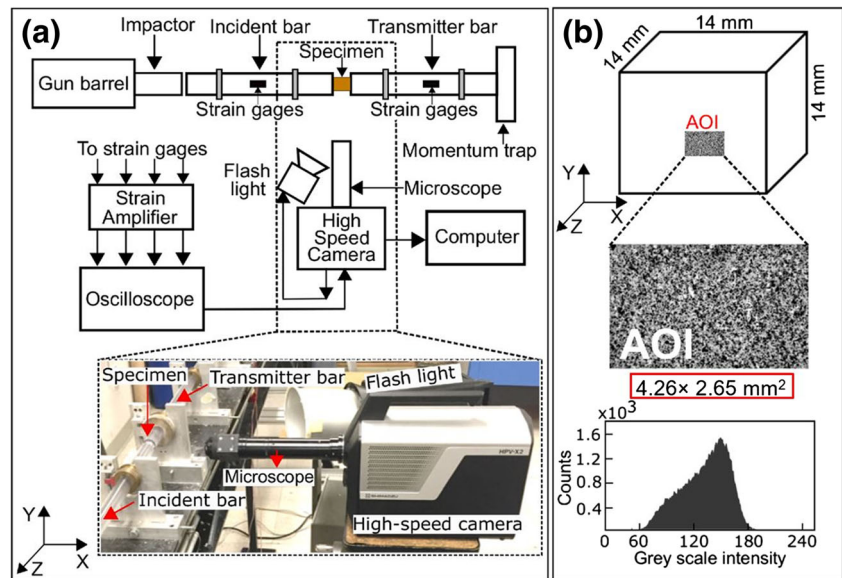
$$\text{Specimen strain rate, } \dot{\epsilon}_s(t) = -\frac{2C_b}{l_0} \epsilon_R(t) \quad (1)$$

$$\text{Strain in the specimen, } \epsilon_s(t) = \int_0^t \dot{\epsilon}_s(t) dt \quad (2)$$

$$\text{Stress in the specimen, } \sigma_s(t) = \frac{E_a A_b}{A_s} \epsilon_T(t) \quad (3)$$

where ' $l_0$ ' is the original length of the specimen, ' $\epsilon_R(t)$ ' is the time-resolved strain from the reflected pulse in the incident bar. ' $C_b = 1470 \text{ m/s}$ ' is the velocity of the sound wave in the polymeric bar, and ' $E_a = 2.5 \text{ GPa}$ ' is the elastic modulus of the bar material. ' $A_b$ ' is the cross-sectional area of the bar, ' $A_s$ ' is the cross-sectional area of the specimen, and ' $\epsilon_T(t)$ ' is the time-resolved strain from the transmitted pulse in the transmitter bar.

**Fig. 1** (a) Schematic description and the actual image of the experimental setup, (b) specimen size, the area of interest (AOI) and its size, typical speckle pattern, and the grayscale intensity curve of the speckles used in this study



For measuring the macroscale and mesoscale full-field strain using DIC, an ultra-high-speed imaging camera HPV-X2 by Shimadzu was used. The full resolution of the camera is  $400 \times 250$  pixel<sup>2</sup> at all framing speeds, with a capability of capturing 128 images. In this study, a framing rate of 0.5–1 million frames/s was selected to capture the complete duration of the dynamic event. Therefore, the total length of the image capturing sequence was 128–256  $\mu$ s. For the macroscale experiments, a 100 mm Tokina lens was used yielding a field of view of  $27.2 \times 17.0$  mm<sup>2</sup> at a resolution close to 68  $\mu$ m/pixel. For the mesoscale measurement, a high magnification far-field microscope by Navitar Inc. was attached to the camera as shown in Fig. 1(a). The field of view of magnification optics was  $4.26 \times 2.65$  mm<sup>2</sup> at a resolution of 10.66  $\mu$ m/pixel. Complete imaging parameters to resolve the sub-grain scale features are given in Table 2. The sample was illuminated with the help of a Photogenic flash lamp (Power light 2500 DR). This lamp takes 200  $\mu$ s to reach full intensity, and then the intensity stays constant for about 1200  $\mu$ s. The triggering of the light was performed from the oscilloscope by considering the full intensity requirement during deformation.

Cubical samples of 14 mm size with the variability of  $\pm 0.2$  mm was used in this study, see Fig. 1(b). The area of

interest (AOI) for strain calculation is shown in Fig. 1(b). Digital image correlation computes the displacement field by tracking the features on the surface of the specimen with a random speckle pattern. In this study, a mesoscale speckle pattern of average size 30–40  $\mu$ m was required. Before speckling, the sample was dry polished using silicon carbide papers with grit sizes varying from ANSI 400–1200 grits, followed by a fine polishing of the specimen using smooth polishing cloths. The area of interest is then marked using the method described in [23]. The microstructural images of the AOI were captured using a VHX microscope, before speckling to later relate the local strain field with the underlying microstructure of the sample. For speckling, first, a base coat of white paint (Rust-oleum-flat white) was applied to the sample. Then before a complete drying of the base coat, a black toner powder (Brother TN-450) was deposited on the surface using an air-brush. The resulting speckle pattern obtained is shown in Fig. 1(b). The greyscale intensity pattern of the speckle follows a bell-shape trend, which is suitable for accurate DIC measurements. For the macroscale experiment, spray paint was used for speckling. A base white coat (Rust-oleum-flat white) was first applied on the sample and then after the complete drying of the white paint, black paint (Rust-oleum-flat black) was

**Table 2** Imaging and post-processing parameters used in this study

Imaging parameters	Post-processing parameters
Imaging lens - Navitar Extension tube	Subset size - $9 \times 9$ pixel <sup>2</sup> ( $96 \times 96$ $\mu$ m <sup>2</sup> )
Lighting- Photogenic flash lamp	Step size - 1
Imaging Framing Rate- 1 Million	Filter Size - 9
Resolution- $400 \times 250$ pixel <sup>2</sup>	Interpolation – Optimized 8-tap
Field of view- $4.26 \times 2.65$ mm <sup>2</sup>	Criterion – ZNSDD
Magnification-10.66 $\mu$ m/pixel	Subset weight – Gaussian weight

sprayed on the top. The average speckle size was calculated using Image J particle analysis module [30] and average speckle size for the macroscale experiments was close to 250–300  $\mu\text{m}$ .

The post-processing of the captured images was performed in VIC-2D, a commercial software by Correlated Solutions Inc. A subset size of  $9 \times 9 \text{ pixel}^2$  ( $96 \times 96 \mu\text{m}^2$ ) was used considering at least  $3 \times 3$  speckles in a subset. Therefore, a crystal of 500  $\mu\text{m}$  spans approximately 25 subsets during the strain calculation. The step size and filter size were chosen to be 1 and 9, respectively. Therefore, a virtual gage length of 9 pixels (96  $\mu\text{m}$ ) was achieved. The matching algorithm was selected to be zero normalized squared difference which is insensitive to the slight illumination intensity variation coming from the flashlight. To convert the digital signal into a continuous data, an optimized 8-tap interpolation function is employed. For the macroscale experiment, a subset size of  $15 \times 15 \text{ pixel}^2$  was used, while the step size and filter size were 1 and 15 respectively.

## Results and Discussion

### Macroscale Stress-Strain Behavior

To verify the force equilibrium in the samples, the transmitted signal (transmitter force) and the sum of incident and reflected signals (incident force) are compared. A typical strain gage signal recorded in the oscilloscope for an experiment conducted on PBS-87 is shown in Fig. 2(a). The sum of the incident and reflected wave signals (incident force) and the transmitter bar signal (transmitter force) appeared to be nearly equal, which indicates that force equilibrium is achieved in the sample [31]. In addition, the image captured during deformation of PBS-87, shown in Fig. 2(b), shows a relatively uniform deformation with negligible barreling effect, which indicates the friction between the sample and bars are negligible. Therefore, the one-dimensional analysis assumption is reasonable and can yield an accurate average stress strain response of the material.

The global average nominal stress, strain and strain rates were calculated from the strain gage signals using equations discussed in “[Experimental Setup, Specimen Geometry, and Data Analysis](#)” Section. Average stress-strain curves and the associated standard deviations calculated from independent experiments for the three set of specimens are shown in Fig. 2. As shown in Fig. 2(c), PBS-80, the lowest mass fraction composite shows a linear viscoelastic response at the beginning of the loading. After the linear deformation, the PBS-80 specimen undergoes a nonlinear transition to the yielding at an applied global strain close to  $\varepsilon_{xx} = 8.5\%$ . The yield stress of the sample was found to be 5.5 MPa. In the post yielding region, region B, nearly a pure plastic response was observed until  $\varepsilon_{xx} = 30\%$ . After strain of  $\varepsilon_{xx} = 30\%$ , region C, the specimen shows significant strain hardening response followed by an ultimate

failure at a strain of about  $\varepsilon_{xx} = 65\%$ . The failure stress for PBS-80 is close to 20 MPa. Interestingly, the stress-strain behavior of PBX-80 was qualitatively very similar to the soft binders under dynamic compression [32, 33]. This suggests that the local binder deformation majorly controlled the behavior of the PBS-80 sample at the beginning of the deformation, followed by stiffening possibly due to the engagement of the crystals in the deformation. On the other hand, PBS-87 and PBS-95 display very distinct response compared to PBS-80. They show a stiffer elastic response at the beginning of the loading (see Fig. 2(d and e)). PBS-87 yields at 11 MPa with a global axial strain of  $\varepsilon_{xx} = 4.8\%$ . The strain at yield and the yield stress of PBS-95 was, 4.1% and 15 MPa, respectively. Both the samples exhibit a softening region after yielding in contrast to PBS-80. The slope of the post-yielding region was high for PBS-95 compared to PBS-87. This indicates that the higher mass fraction sample (PBS-95) shows lower resistance to the failure after yielding compared to PBS-87. The stress-strain behavior of PBS-87 and PBS-95 are qualitatively very similar to the behavior of quasi-brittle materials indicating a stronger granular effect on the material deformation. The stress-strain response shows that the global material behavior is significantly affected by the mass fraction of the composite. The mass fraction between 80 and 87% can be considered as a transition region where the material behavior changes from a soft binder dominated material behavior to crystal deformation governed brittle behavior. Unfortunately, a mass fraction increment that is smaller than 5% would bring ambivalent result due to experimental statistical margin, therefore, pinpointing the exact mass fraction at which the transition occurs was difficult to obtain from the experiments.

In this experimental study, 2D DIC was used; thus, only the two principal strain components were available. The von Mises strain is calculated using the equation  $\varepsilon_{von} = \sqrt{(\varepsilon_1^2 + \varepsilon_2^2 - \varepsilon_1\varepsilon_2)}$ . The strain components and the von Mises strain of the three samples at three global axial strains are given in Table 3. The table shows both the mean and the associated standard deviation (SD). The standard deviation is small (below 10%) for all cases, indicating the measurement accuracy is very good. The von Mises strain field for the three mass fractions shows different deformation pattern at various global axial strains. The full field von Mises strain evolution and the strain components at a global axial strain of  $9.9 \pm 0.2\%$  for the three mass fractions samples are shown in Fig. 3.

In PBS-80, the von Mises strain at a low global axial strain is small, and the localization appears at lower number of locations compared to PBS-87 and PBS-95. As the applied strain increases, multiple bands are observed in all the specimens (see the white dotted lines and the arrows). At a higher applied strain, the bands are visible in PBS-87 and PBS-80 but tend to disappear in PBS-95 due to more strain localized regions. The component strain field, in all the three mass fractions shows

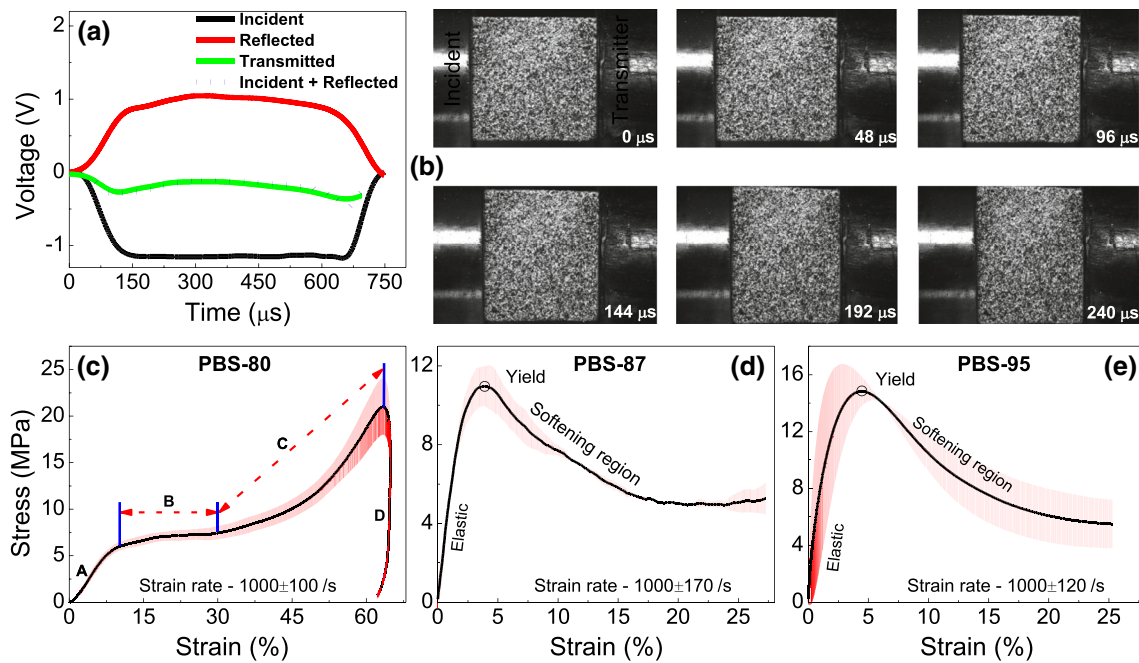


**Fig. 2** (a) Representative oscilloscope signal obtained for PBS-87, (b) raw images of PBS-87 during deformation, the nominal stress–strain curve for three different mass fractions, (c) PBS-80, (d) PBS-87 and (e) PBS-95. Error bars are shown to indicate variability in three separate experiments

strong strain localization during loading. Macroscopically shear localization is apparent for all the three mass fractions (see shear strain field marked with ovals and dotted lines), at the same time lateral strains are also significantly high. This indicates that the dilation also plays a significant role in the final shear failure of the sample. This type of dilative shear localization is observed in the sand under low confinement pressures [34]. It is important to note that the crystal fractures in the dilative type shear bands would be less compared to the compaction type shear bands.

To understand the dilation and quantify the damage evolution in PBS, volumetric strain was calculated from the full-field strain data. A zero volumetric strain corresponds to incompressible binder dominated deformation, a negative volumetric strain corresponds to compaction and a positive volumetric strain corresponds to dilation. To calculate the volumetric strain, three components of

the strains are required. However, the DIC calculation on the surface of the sample can only measure in-plane components  $\epsilon_{xx}$  and  $\epsilon_{yy}$ . To obtain the third component  $\epsilon_{zz}$ , another camera was used looking at the top surface of the specimen, giving  $\epsilon_{zz}$  and  $\epsilon_{xx}$ . Due to an isotropy nature of the material, the lateral strain in both sides is obtained to be nearly equal  $\epsilon_{zz} \approx \epsilon_{yy}$ . Hence, the volumetric strain is calculated using the following equation,

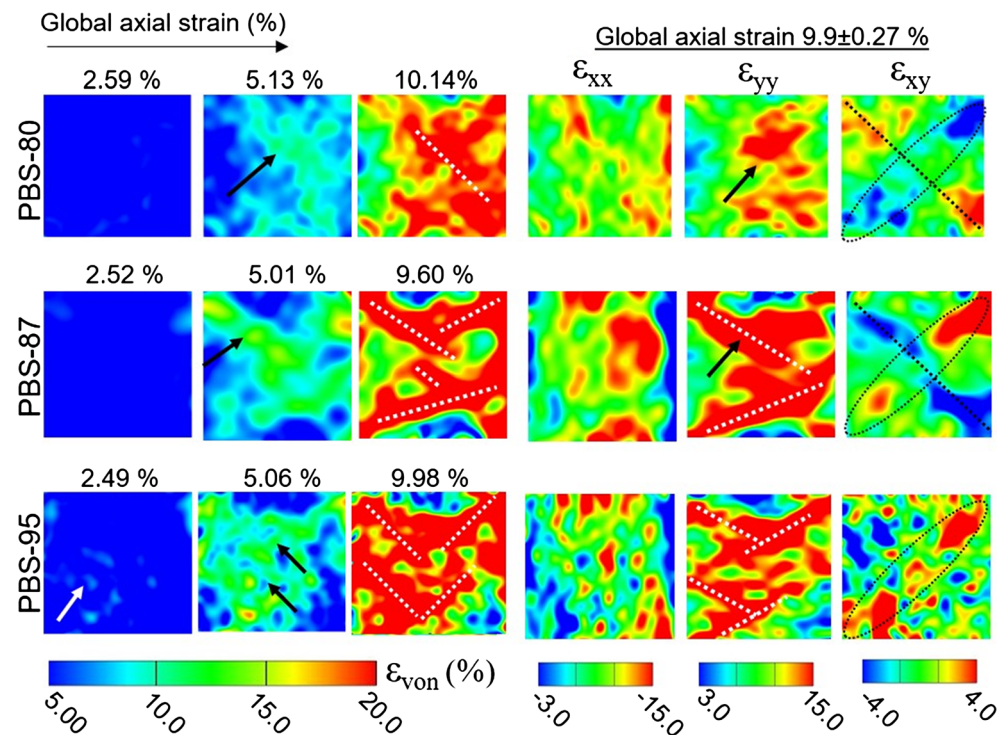
$$\epsilon_{vol} = (1 + \epsilon_{xx})(1 + \epsilon_{yy})^2 - 1 \tag{4}$$

The soft binder in this material is nearly incompressible, and on the other hand, the sugar crystals are highly brittle in nature. Therefore, the volumetric strain measurement in a specimen can be used to identify the onset of damage in the composite specimen and the corresponding dominant failure mode which cause the dilation in the sample [35].

**Table 3** Mean and standard deviation of von Mises and component strains for three global axial strains shown in Fig. 3

Sample	Exx (mean (SD)) (%)	Eyy (mean (SD)) (%)	Exy (mean (SD)) (%)	Evon (mean (SD)) (%)
PBS-80	2.59 (0.5)	0.90 (0.3)	0.00 (.03)	3.20 (0.6)
	4.96 (0.9)	2.38 (1.6)	0.03 (0.8)	8.60 (2.5)
	9.34 (6.2)	7.12 (2.5)	0.37 (1.3)	15.3 (2.9)
PBS-87	2.52 (0.6)	1.45 (0.5)	0.00 (.03)	3.50 (0.8)
	5.01 (1.3)	4.75 (1.6)	0.03 (0.8)	8.60 (2.5)
	9.60 (6.2)	12.5 (6.8)	0.35 (3.6)	20.3 (8.4)
PBS-95	2.49 (1.9)	1.61 (1.3)	0.15 (1.1)	4.44 (2.2)
	5.06 (3.3)	4.18 (3.1)	0.26 (1.7)	9.33 (4.1)
	9.98 (6.4)	11.1 (7.7)	0.50 (3.5)	21.2 (9.2)

**Fig. 3** The von Mises strain field at different applied global strain and components strain field at a global axial strain of  $9.9 \pm 0.27\%$ , for PBS-80, PBS-87, and PBS-95



The volumetric strain and the stress evolution in the sample for all the three different mass fractions are shown in Fig. 4. A negative volumetric strain is observed in the beginning until about  $100 \mu\text{s}$ , indicating the collapse of voids/cracks present in the sample. As shown in Fig. 4(b), the negative volumetric strain is pronounced in PBS-80, indicating the pore collapse is relatively easier in lower loading compared to high mass fraction samples. To collapse the same number of voids in the high solid fraction samples, significantly high amount of energy may be required due to the high probability of crystal to crystal contacts enclosing the voids. The small negative volumetric strain observed in PBS-95 is an evidence of the stated deformation mechanism for high solid loading.

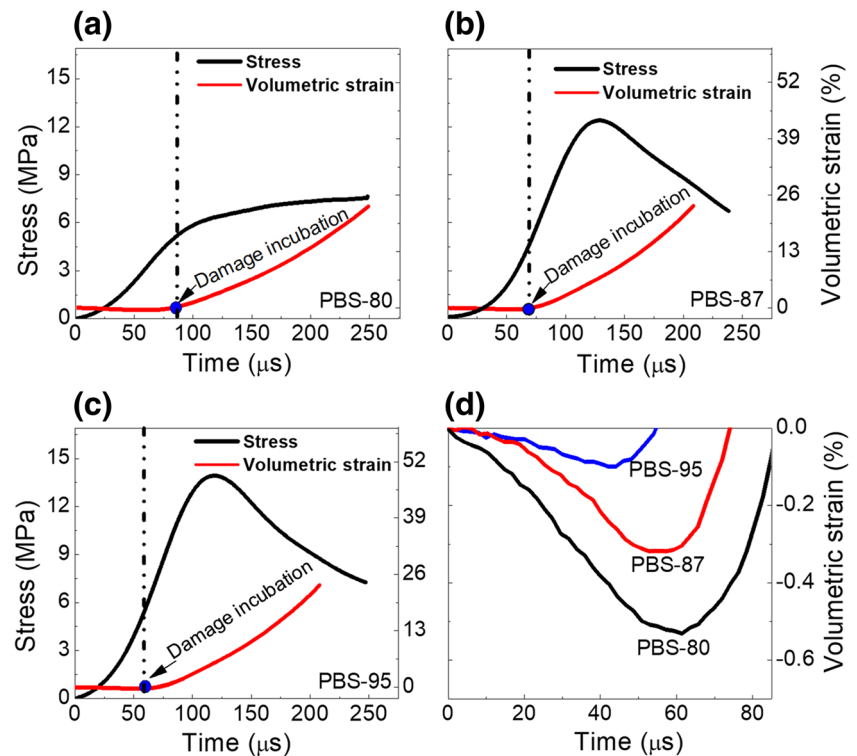
The increase in volumetric strain as a function of loading time indicates damage initiation is occurring in the material. For PBS-80, the stress at which the damage initiated is close to  $5.7 \text{ MPa}$ , a value very close to the yielding of the sample. For PBS-87 and PBS-95, the volumetric strain increases nonlinearly due to the early damage accumulation in the sample. The damage evolution in PBS-87 started far before the yield point in contrast to PBS-80, showing that the higher solid fraction sample has lower resistance to failure. PBS-95 also shows a very similar response and even exhibits an earlier damage initiation compared to PBS-87. This indicates that for higher solid loading, the local damage is initiated earlier due to either force chain formation mechanism or other crystal failure modes. To further probe into the local deformation that yields such a macroscopic behavior, mesoscale experiments were conducted and discussed in the next section.

### Mesoscale Strain Heterogeneity in PBS-80, PBS-87, and PBS-95

It should be noted here that the mesoscale measurements were conducted up to an average global strain of  $3\%$ . Beyond that, the images were not in focus due to a limitation in the depth of field at high magnifications. Therefore, the local strain components in the initial phase of the loading are given, especially, before the yielding of the sample. In addition, to compare the local strain field with the underlying microstructure, the local strain contours are plotted in the undeformed coordinates.

The contour plots of the in-plane local von Mises strain field for PBS-80, PBS-87, and PBS-95 at three global strains are shown in Fig. 5(a). A highly heterogeneous strain field is apparent for all the material compositions used in this study. Also, the strain heterogeneity appears to be increasing with an increase in applied load. To compare the local strain field with the microstructure of the sample, the images of the underlying microstructure and the strain localization region of the interests are marked as shown in Fig. 5(a and c). Interestingly, the von Mises strain field in PBS-80 is concentrated at some local areas, whereas the von Mises strain field in PBS-87 and PBS-95 is more spread out with significantly high strains. For example, in PBS 80, the strain localization is mainly constrained in the polymer binder (region 1, 2, 3 and 4) whereas, PBS-87 and PBS-95 show a significantly higher number of locations with local strain, see region 5, 6, 7, 8, and 9. This is the direct

**Fig. 4** The volumetric strain and stress with time for three different mass fractions, (a) PBS-80, (b) PBS-87 and (c) PBS-95, (d) the volumetric strain zoomed in before  $t = 80 \mu\text{s}$  which shows the negative volumetric strain



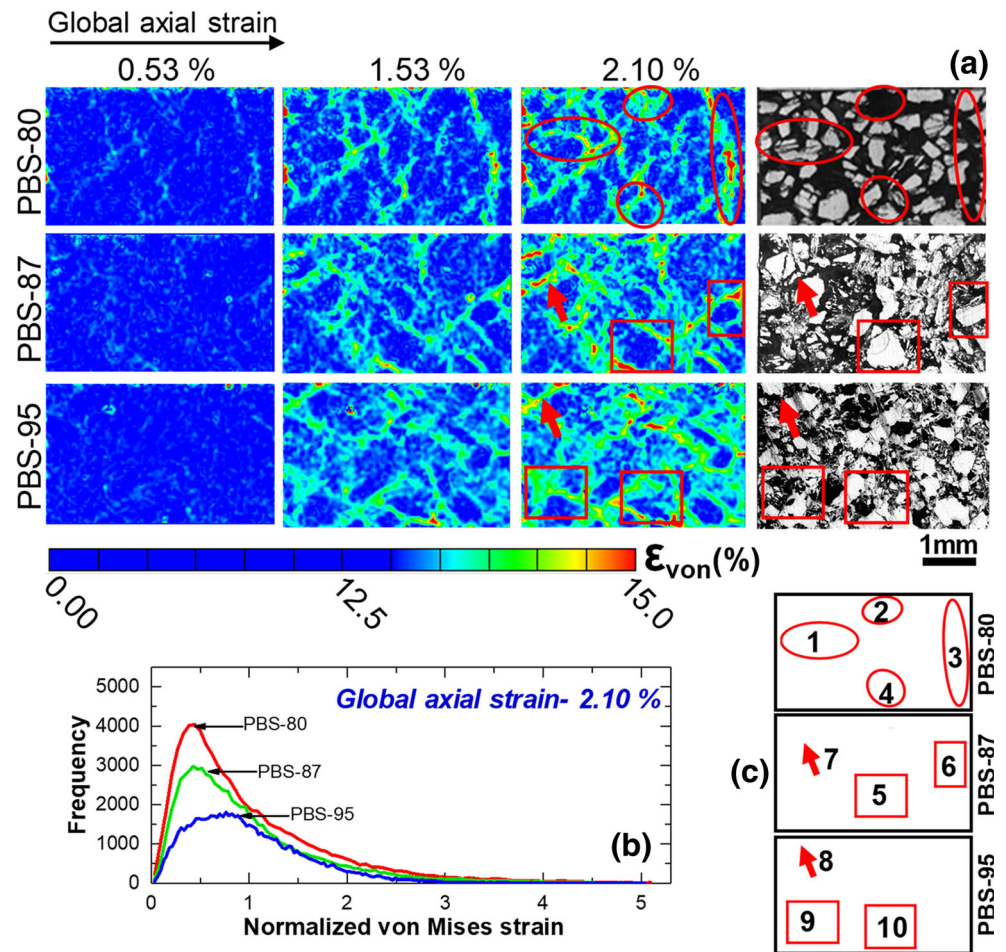
consequence of the higher mass fraction in the material. The higher mass fraction increases the number of contacts between the crystals. Therefore, the deformation of PBS-95 will be mainly governed by the crystal deformation.

Figure 5(b) shows the histogram of the normalized von Mises strain. It is evident that for all the samples, the histogram is right skewed, indicating that the high strain values profoundly influence the average strain in the area of interest. It is presumable that PBS-80 contains a more significant proportion of polymer binder leading to a lower number of crystal-to-crystal contacts compared to PBS-87 and PBS-95. This is evident from the microstructure shown in Fig. 5(a). Thus, the deformation behavior in PBS-80 is majorly controlled by the polymer deformation in the initial deformation phase. Consequently, PBS-80 has a steeper histogram with peak farthest from the mean ( $\overline{\varepsilon_{von}} = \varepsilon_{von} / (\varepsilon_{von})_{mean} = 1$ ), indicating a small number of localized regions. Comparing the microstructure with the von Mises strain field, it can be seen that the strain localization is observed only in the binder. This results in higher damage tolerance in PBS-80 as seen in the stress-strain response. The increase in mass fraction creates a higher number of crystal contacts essentially resulting in a more dispersed deformation field with many localized regions occurring due to force transfer between the crystals. PBS-87 has a slightly broader histogram indicating a higher number of high strain localization regions compared to PBS-80. Whereas, the strain histogram of PBS-95 does not have a sharp peak like PBS-80 or PBS-87, instead, relatively a flat peak due to a higher number of localized strain regions. As a

result, the peak of the histogram moves closer to the mean as seen in Fig. 5(b). To better understand the local deformation mechanism that causes such features, the local strain field is investigated as discussed below.

The local contour plot of the strain fields at a global strain of 2.1% for the three-different material compositions, are shown in Fig. 6. It is important to note that in all cases, the axial strain localization occurs at the vertical interfaces of the crystal where polymer binder separates one crystal from another. As shown in the figure, the local compressive strain is higher than 10% for a global strain of 2.1%. It is also observed that new sites of strain localization are formed with the increase in load. Unlike, the axial strain, in this case, the local transverse strain localization occurs in small bands at about  $45^\circ$  with the loading axes, indicating a local dilation in the material. These local dilation locations are mainly the polymer-rich regions in the case of PBS-80, see (ovals 1, 2 and 3). Therefore, delamination would be a significant damage initiation mechanism in PBS-80. Whereas, in PBS-87 and PBS-95 the high local transverse strains are observed on the crystals and an interface between the crystals and binder (see the marked boxes in PBS-87 and PBS-95). Also, the local transverse strain is highly localized in the case of the highest mass fraction (PBS-95) compared to other compositions. These localizations could be associated with the fracture of the crystal due crystal-to-crystal contact and stress concentration at the contact points. Interestingly, the local shear strain is seen to be localized in the highly deforming polymer-rich region in case of PBS-80, and in the crystal fracture locations

**Fig. 5** (a) Local von Mises strain at different axial global strains for PBS-80, PBS-87 and PBS-95 along with the underlying microstructure (specific locations are marked) (b) histogram of the von Mises strain normalized with the average von Mises strain at a global axial strain of 2.10% for PBS-80, PBS-87 and PBS-95. (c) numbering of the oval, arrow and rectangular marking used for highlighting specific local regions in area of interest



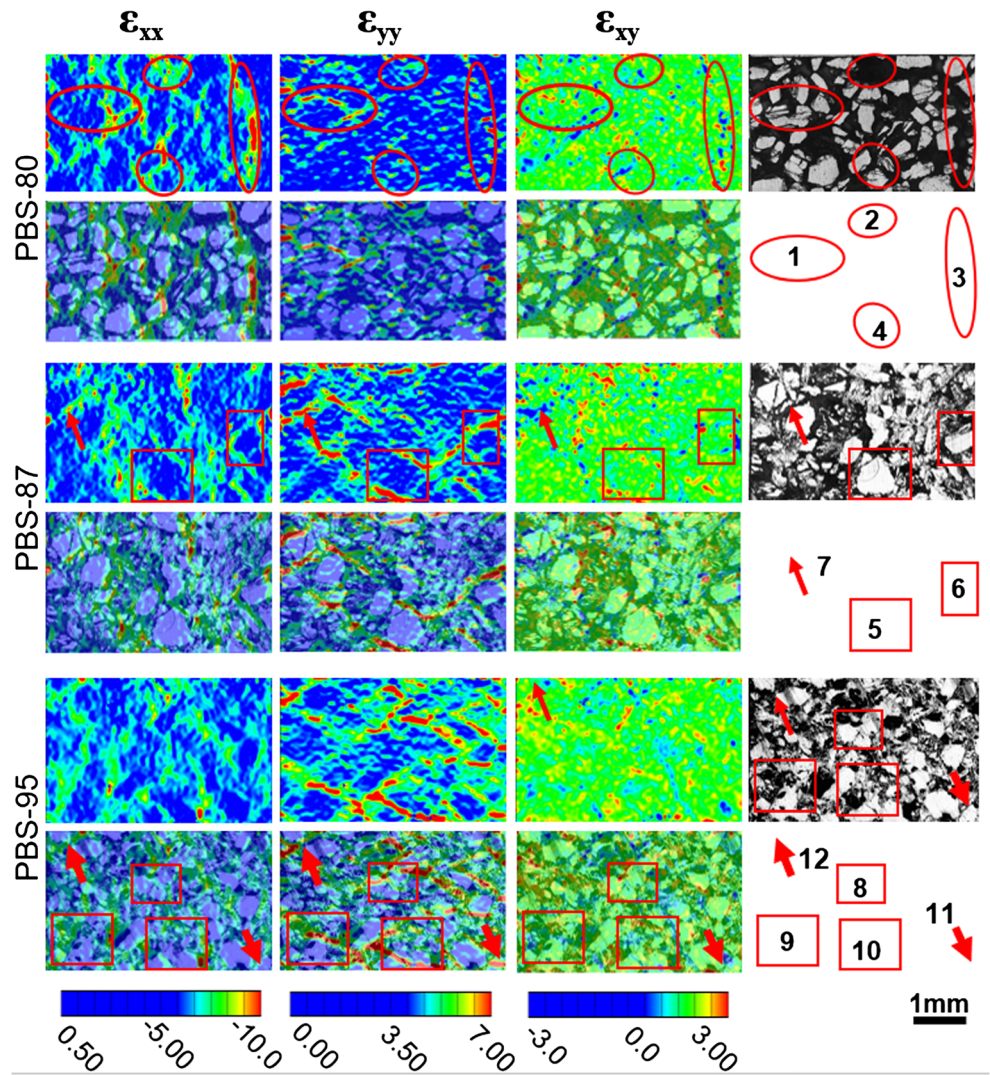
and polymer rich regions (see region 5, 8 and 10) in the case of PBS-87 and PBS-95. These local fracture propagation and coalescence is easier in the high mass fraction composite compared to low mass fraction composite because the crack propagation in soft binder composite is hindered due to the high toughness of the soft binder. Comparing the damage initiation in PBS-80, PBS-87, and PBS-95, lower mass fraction PBS samples shows higher resistance in developing damage due to high soft polymer content. On the other hand, PBS-87 and PBS-95 show lower strength to the damage incubation. This is because the small amount of polymer causes the crystals to engage in the primary load transfer, thereby, the crystals deform, fracture and de-bonds from the polymer binder. To see the damage localization with respect to the position of the crystals, an overlay plot of the transverse strain on the microstructure is presented in Fig. 7.

The images in Fig. 7 are created by making the contour plot transparent for all strains below 3%. Therefore, the transparent part has strain lower than 3%. It essentially shows the regions in PBS-80, PBS-87, and PBS-95 with high lateral strain. As discussed in the previous section, it is clear that a high tensile strain region is more extensive and scattered in PBS-95 compared to PBS-87 and PBS-80. In PBS-80, the high tensile

strain is highly localized in small locations. In both PBS-87 and PBS-95 crystal, fracture locations are visible, whereas in PBS-80 the crystal fracture locations are not present in the initial phase of loading. Therefore, failure initiation in PBS-80 is mainly due to de-bonding of the binder from the crystal. In the post yielding region, the damage incubation can result in the formation of macro-cracks and eventually lead to failure. On the other hand, PBS-87 and PBS-95 failed because of a combined mechanism of crystal fracture and polymer binder de-bonding. This is the primary failure mode of the quasi-brittle behavior of the material. It is essential to note that, the fracture stress of the sugar crystals is close to 200 MPa. However, in this experiment, there is clear evidence of the crystal fracture in PBS-95 despite low failure stress of 16 MPa. It is well-known that force chains play an essential role in the strain localization and damage behavior of granular composites. PBX is a cohesive granular media. It is shown that the cohesive granular assemblies can have the force chains very similar to granular material. Rajdai et al. showed that the force distribution in a cohesive granular media has an exponential tail [36]. This means the forces in the crystals that involved in the load transfer mechanism may have caused the fracture due to stress concentration.



**Fig. 6** Local axial, transverse and shear strain at an axial global strain of 2.1% for PBS-80, PBS-87, and PBS-95 along with the underlying microstructure (specific locations are marked). Strain field overlaid on top of the microstructure, and the numbering of the marking is also shown



**Summary**

A multiscale experimental investigation was performed to understand the effect of the mass fraction on the damage evolution in particulate polymer composites subjected to dynamic

loading. PBS with three different mass fractions loading PBS-80, PBS-87, and PBS-95 is considered. The experimental study shows that the low mass fraction sample, PBS-80, shows relatively very soft material behavior. As the mass fraction increases, a transition from soft polymer stress-strain

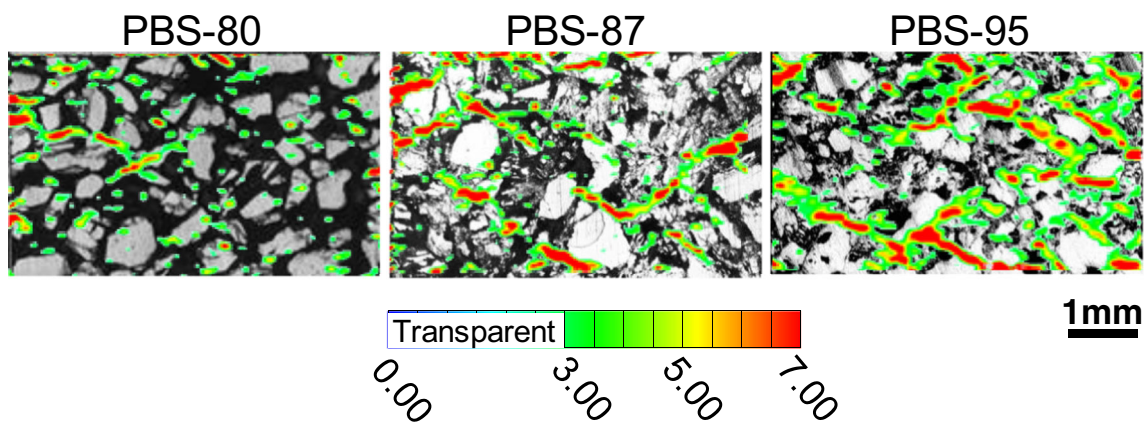


**Fig. 7** The overlaid lateral strain contour plot showing only high transverse strain (strains lower than 3% are made transparent)

behavior to a quasi-brittle type stress-strain behavior is observed. The mass fraction between 80 and 87% may be considered as a critical mass fraction for the transition of soft material dominated behavior to brittle material behavior. The mesoscale experiments reveal that the soft material behavior is solely due to a low mass fraction and a delayed engagement of crystals in the deformation of the sample. In contrast, the brittle type behavior of PBS-87 and PBS-95 is due to the crystal fracture which causes local instabilities that give rise to fracture coalescence and final failure in a short time. It also indicates that the deformation mechanism is not only governed by the brittleness of the binder at a higher strain rate but is also derived by the engagement of the crystal in the force transfer during deformation. The study indicates that the prediction of local deformation material behavior of PBX with different solid loading may require different types of material model. For low mass loading, soft binder material models could be sufficient to capture the elastic-plastic behavior, on the other hand for the high mass fraction, models that are used for the quasi-brittle materials may be needed.

**Acknowledgments** The financial support of Air Force Office of Scientific Research (AFOSR) under Grant No. FA9550-14-1-0209 and FA9550-16-1-0623 is gratefully acknowledged.

## References

1. Yan Q-L, Zeman S, Elbeih A (2012) Recent advances in thermal analysis and stability evaluation of insensitive plastic bonded explosives (PBXs). *Thermochim Acta* 537:1–12
2. Tarver CM, Tran TD (2004) Thermal decomposition models for HMX-based plastic bonded explosives. *Combust Flame* 137:50–62
3. Balzer JE, Siviour CR, Walley SM et al (2004) Behaviour of ammonium perchlorate-based propellants and a polymer-bonded explosive under impact loading. *Proc R Soc A Math Phys Eng Sci* 460:781–806. <https://doi.org/10.1098/rspa.2003.1188>
4. Grantham SG, Siviour CR, Porud WG, Field JE (2004) High-strain rate Brazilian testing of an explosive simulant using speckle metrology. *Meas Sci Technol* 15:1867
5. Barua A, Horie Y, Zhou M (2012) Microstructural level response of HMX–Estane polymer-bonded explosive under effects of transient stress waves. *Proc R Soc Lond A Math Phys Sci* 2147:3725–3744.
6. Drodge DR, Williamson DM (2016) Understanding damage in polymer-bonded explosive composites. *J Mater Sci* 51:668–679
7. Siviour CR, Grantham SG, Williamson DM et al (2009) Novel measurements of material properties at high rates of strain using speckle metrology. *Imaging Sci J* 57:326–332
8. Kang G, Chen P, Guo X et al (2018) Simulations of meso-scale deformation and damage of polymer bonded explosives by the numerical manifold method. *Eng Anal Bound Elem* 96:123–137
9. Gao X, Zhao T, Luo G et al (2018) Enhanced thermal and mechanical properties of PW-based HTPB binder using polystyrene (PS) and PS–SiO<sub>2</sub> microencapsulated paraffin wax (MePW). *J Appl Polym Sci* 135:46222
10. Wang X, Wu Y, Huang F (2017) Numerical mesoscopic investigations of dynamic damage and failure mechanisms of polymer bonded explosives. *Int J Solids Struct* 129:28–39
11. You S, Chen M-W, Dlott DD, Suslick KS (2015) Ultrasonic hammer produces hot spots in solids. *Nat Commun* 6:6581
12. Roberts ZA, Casey AD, Gunduz IE et al (2017) The effects of crystal proximity and crystal-binder adhesion on the thermal responses of ultrasonically-excited composite energetic materials. *J Appl Phys* 122:244901
13. Chen M-W, You S, Suslick KS, Dlott DD (2014) Hot spots in energetic materials generated by infrared and ultrasound, detected by thermal imaging microscopy. *Rev Sci Instrum* 85:023705. <https://doi.org/10.1063/1.4864197>
14. Roessig KM (2002) Mesoscale mechanics of plastic bonded explosives. In: AIP conference proceedings. IOP INSTITUTE OF PHYSICS PUBLISHING LTD, pp 973–978
15. Field JE (1992) Hot spot ignition mechanisms for explosives. *Acc Chem Res* 25:489–496
16. Hu Z, Luo H, Bardenhagen S et al (2015) Internal deformation measurement of polymer bonded sugar in compression by digital volume correlation of tomography. *Exp Mech* 1:289–300
17. Beckvermit JC, Peterson JR, Harman T et al (2013) Multiscale modeling of accidental explosions and detonations. *Comput Sci Eng* 15:76–86
18. Barua A, Zhou M (2011) A Lagrangian framework for analyzing microstructural level response of polymer-bonded explosives. *Model Simul Mater Sci Eng* 19:55001
19. Barua A, Horie Y, Zhou M (2012) Energy localization in HMX–Estane polymer-bonded explosives during impact loading. *J Appl Phys* 111:54902
20. Bardenhagen SG, Brackbill JU, Sulsky D (2000) Numerical study of stress distribution in sheared granular material in two dimensions. *Phys Rev E* 62:3882
21. LaBarbera DA, Zikry MA (2015) Dynamic fracture and local failure mechanisms in heterogeneous RDX–Estane energetic aggregates. *J Mater Sci* 50:5549–5561
22. LaBarbera DA, Zikry MA (2015) Heterogeneous thermo-mechanical behavior and hot spot formation in RDX–estane energetic aggregates. *Int J Solids Struct* 62:91–103
23. Ravindran S, Tessema A, Kidane A (2016) Local deformation and failure mechanisms of polymer bonded energetic materials subjected to high strain rate loading. *J Dyn Behav Mater* 2:146–156. <https://doi.org/10.1007/s40870-016-0051-9>
24. Ravindran S, Tessema A, Kidane A (2017) Multiscale damage evolution in polymer bonded sugar under dynamic loading. *Mech Mater* 114:97–106
25. Ravindran S, Tessema A, Kidane A (2016) Note: dynamic meso-scale full field surface deformation measurement of heterogeneous materials. *Rev Sci Instrum* 87:036108. <https://doi.org/10.1063/1.4944488>
26. Ravindran S, Tessema A, Kidane A, Sutton MA (2016) Meso-scale deformation mechanisms of polymer bonded energetic materials under dynamic loading. In: Conference proceedings of the society for experimental mechanics Series, pp 451–456
27. Parab ND, Roberts ZA, Harr MH et al (2016) High speed X-ray phase contrast imaging of energetic composites under dynamic compression. *Appl Phys Lett* 109:131903
28. Ravindran S, Tessema A, Kidane A, Sutton MA (2016) Meso-scale deformation mechanisms of polymer bonded energetic materials under dynamic loading. In: Mechanics of composite and multifunctional materials, vol 7. Springer, pp 451–456
29. Bacon C (1998) An experimental method for considering dispersion and attenuation in a viscoelastic Hopkinson bar. *Exp Mech* 38:242–249
30. Schindelin J, Arganda-Carreras I, Frise E et al (2012) Fiji: an open-source platform for biological-image analysis. *Nat Methods* 9:676
31. Chen W, Zhang B, Forrestal MJ (1999) A split Hopkinson bar technique for low-impedance materials. *Exp Mech* 39:81–85



32. Jordan JL, Montaigne D, Gould P et al (2016) High strain rate and shock properties of hydroxyl-terminated polybutadiene (HTPB) with varying amounts of plasticizer. *J Dyn Behav Mater* 2:91–100
33. Kendall MJ, Drodge DR, Froud RF, Siviour CR (2014) Stress gage system for measuring very soft materials under high rates of deformation. *Meas Sci Technol* 25:75603
34. Alikarami R, Torabi A (2015) Micro-texture and petrophysical properties of dilation and compaction shear bands in sand. *Geomech Energy Environ* 3:1–10
35. Lazzeri A, Thio YS, Cohen RE (2004) Volume strain measurements on CaCO<sub>3</sub>/polypropylene particulate composites: the effect of particle size. *J Appl Polym Sci* 91:925–935
36. Radjai F, Topin V, Richefeu V et al (2010) Force transmission in cohesive granular media. In: *Math model phys instances granul flows*, pp 240–260

**Publisher's Note** Springer Nature remains neutral with regard to jurisdictional claims in published maps and institutional affiliations.

